JACS
JOURNAL OF THE AMERICAN CHEMICAL SOCIETY
Article
pubs.acs.org/JACS

Hydroxide Solvation and Transport in Anion Exchange Membranes

Chen Chen,[†,‡] Ying-Lung Steve Tse,[†,⊥] Gerrick E. Lindberg,[§] Chris Knight,[∥] and Gregory A. Voth*[,†]

[†]Department of Chemistry, James Franck Institute, Institute for Biophysical Dynamics, and Computation Institute, The University of Chicago, Chicago, Illinois 60637, United States

[‡]College of Chemistry and Molecular Sciences, Hubei Key Lab of Electrochemical Power Sources, Wuhan University, Wuhan 430072, China

[§]Department of Chemistry and Biochemistry, Northern Arizona University, Flagstaff, Arizona 86011, United States

[∥]Leadership Computing Facility, Argonne National Laboratory, Argonne, Illinois 60439, United States

Supporting Information

ABSTRACT: Understanding hydroxide solvation and transport in anion exchange membranes (AEMs) can provide important insight into the design principles of these new membranes. To accurately model hydroxide solvation and transport, we developed a new multiscale reactive molecular dynamics model for hydroxide in aqueous solution, which was then subsequently modified for an AEM material. With this model, we investigated the hydroxide solvation structure and transport mechanism in the membrane. We found that a relatively even separation of the rigid side chains produces a continuous overlapping region for hydroxide transport that is made up of the first hydration shell of the tethered cationic groups. Our results show that hydroxide has a significant preference for this overlapping region, transporting through it and between the AEM side chains with substantial contributions from both vehicular (standard diffusion) and Grotthuss (proton hopping) mechanisms. Comparison of the AEM with common proton exchange membranes (PEMs) showed that the excess charge is less delocalized in the AEM than the PEMs, which is correlated with a higher free energy barrier for proton transfer reactions. The vehicular mechanism also contributes considerably more than the Grotthuss mechanism for hydroxide transport in the AEM, while our previous studies of PEM systems showed a larger contribution from the Grotthuss mechanism than the vehicular mechanism for proton transport. The activation energy barrier for hydroxide diffusion in the AEM is greater than that for proton diffusion in PEMs, implying a more significant enhancement of ion transport in the AEM at elevated temperatures.

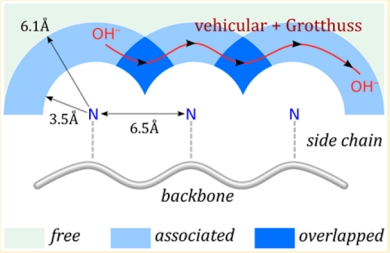

1. INTRODUCTION

Anion exchange membranes (AEMs) are solid anion-conducting polymer electrolytes that contain positively charged side chains covalently bound to or embedded in a polymer backbone.[1−3] The counterparts of AEMs are the more well known proton exchange membranes (PEMs), which carry bound anionic side chains and conduct protons instead.[4] Compared with AEMs, PEMs have a longer history and have received stronger commercial interest, leading to wider application in electric energy conversion and storage.[5,6] However, for stability and efficiency considerations, PEMs usually require the use of platinum-containing catalysts because of the highly acidic nature of the membrane, and thus, their expense often hinders more widespread applications.[5,7,8] In contrast, the alkaline environment in an AEM allows for the use of non-noble-metal catalysts, which could potentially lead to the next generation of fuel cell technologies at lower cost.[9−11]

In the past two decades, there has been rapid growth in research interest in AEMs,[1−3,8,12−15] but the overall performance (conductivity, mechanical strength, chemical stability, etc.) is generally inferior to that of PEMs such as Nafion. Rational design of such materials requires a better understanding of their intrinsic structures and the underlying ion transport mechanisms. Computer simulations and theoretical models can provide useful insights into these properties,[16−19] yet these tools have only recently been applied to understand AEMs.[8,20−24] In 2012, Pan et al.[8] presented some preliminary simulation results on quaternary ammonium polysulfone (QAPS) showing percolating ionic channels and distinct cation and hydroxide distributions at different hydration levels. In late 2013, the same group employed a coarse-grained simulation to study the morphologies of four different modified versions of QAPS[20] and were able to identify a material with optimal (wide and percolated) ionic channels by screening from all of the modified candidates. Following this prediction, the synthesized materials showed promising performance, and the small-angle X-ray scattering results agreed well with the calculated structure factors from simulations. In 2014, we reported classical simulations of a poly(vinyl benzyltrimethylammonium) (PVBTMA) system[21] showing a novel "co-ion effect" in which Cl^- can significantly enhance the F^- mobility in the membrane, and in a subsequent work on aqueous ionic systems,[22] we demonstrated the generality of this phenomenon. Also in 2014, Han et al.[23] compared results for AEMs and PEMs based on the polysulfone backbone and managed to

Received: November 15, 2015
Published: December 30, 2015

DOI: 10.1021/jacs.5b11951
J. Am. Chem. Soc. 2016, 138, 991−1000

rationalize the distinct diffusion constants of the two classes of membranes from the perspective of ionic group solvation and free ion correlation. In 2015, Herbst et al.[24] reported a theoretical study of the spatial distribution of absorbed water in a diblock AEM material. Their calculations predicted a nearly uniform distribution of water under most normal operating conditions, but under certain conditions, when there is phase separation between the hydrophilic blocks and water, the membrane conductivity can be enhanced.

The solvation and transport of hydroxide in hydrated environments is influenced by the Grotthuss (proton hopping) mechanism.[25] In this mechanism for hydroxide, excess negative charge is shuttled through a chain of water molecules by means of a series of O−H bond breaking and formation processes. Conventional classical molecular dynamics (MD) approaches based on empirical force fields are not capable of describing Grotthuss shuttling because they do not allow for changes in the chemical bonding topology. Ab initio molecular dynamics (AIMD), which treats the electronic degrees of freedom explicitly, might seem to be a natural choice for this purpose,[26] but the significant computational cost restricts its application to relatively small systems and short time scales. One possible solution to such a problem is the multistate empirical valence bond (MS-EVB) algorithm.[27,28] In the MS-EVB framework, various resonance structures are defined as basis states, and these are coupled to each other to form the overall Hamiltonian matrix. Each diagonal element in the matrix contains information about the bonded and nonbonded interaction energies for the basis state of the system corresponding to a given bonding topology, while each off-diagonal element contains a coupling term between basis states that share a proton. The states in an MS-EVB algorithm are able to dynamically adopt different bonding configurations in response to changes in the environment with much less computational expense than AIMD. This higher computational efficiency makes MS-EVB suitable for the study of more complicated systems in condensed phases, such as proton transport in polymer electrolyte membranes.[19,29−31] The MS-EVB approach can also be generalized to treat multiple excess protons or hydroxides.[32] To emphasize the multiscale nature of this methodology, we shall call all of these models multiscale reactive molecular dynamics (MS-RMD) models because their parameters can in principle be directly obtained from electronic structure forces.[33]

The remainder of this paper is organized as follows: In section 2, the simulation details are reviewed briefly. In section 3, extensive characterizations of bulk and PVBTMA systems are presented, and on the basis of these results, a hydroxide transport mechanism in the PVBTMA system is proposed. Finally, in section 4 we summarize the work and comment on the future directions.

2. SIMULATION DETAILS

In this work, we parametrized a new reactive model for hydroxide (MS-RMD-OH) in water against AIMD reference data. The model was then combined with the general AMBER force field (GAFF)[34] to produce a reactive model for PVBTMA, which constitutes the hydrophilic part in some random or block copolymers.[35−38]

Two different classes of systems were investigated: hydroxide transport in bulk water and in a PVBTMA membrane. We constructed four systems for parametrization and subsequent characterization, details of which are shown Table 1. It should be noted that the PVBTMA configurations used in the AIMD simulations (for details, see the Supporting Information (SI)) and parametrizations were at a different hydration level (λ = 9, where λ is defined as the number of water molecules per OH^-) than in the MS-RMD simulations (λ = 14).

Table 1. Systems and Their Components

	number of each component		
system name	PVBTMA (number of monomers)	OH^-	H_2O
bulk-s[a]	0	1	127
bulk	0	1	255
PVBTMA-s[a]	10	10	90
PVBTMA	40	40	560

[a]Systems used in AIMD simulation and parametrization. These systems are smaller and are labeled with the suffix "-s".

The chemical structure of PVBTMA used in the present work is shown in Figure 1, and each polymer chain contained 10 monomers (n = 10 in Figure 1). In most of this work, we studied systems with four such 10-mer chains at λ = 14, corresponding to the experimentally fully hydrated state of a recently studied AEM made of a block copolymer with PVBTMA and poly(tetrafluoroethylene) as the hydrophilic and hydrophobic blocks, respectively.[38] Systems at the lower hydration levels were used only to study the equilibrated density in the following section. We also tested the robustness of our results by studying a system that was larger by a factor of 3 and systems with the same number of monomers in total but with different chain lengths (e.g., two chains each with 20 monomers or eight chains each with five monomers) to ensure that system size effects would not change the overall conclusions. In Table S1 we define all of the atom types that will be mentioned throughout this paper.

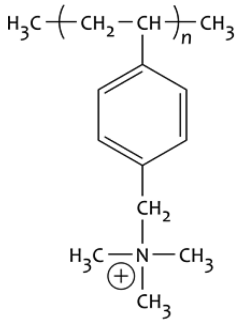

Figure 1. Structure of poly(vinyl benzyltrimethylammonium) (PVBTMA).

In the following part of this section, we briefly discuss the method used. The list of simulation parameters, the parametrization, and more detailed information can be found in the SI.

The simulations were performed using a modified version of LAMMPS[39] in which our own module was used for the MS-EVB calculations. The snapshots of trajectories were prepared using VMD.[40] When multiple reaction complex (here OH^-) systems were simulated, the self-consistent iterative MS-EVB (SCI-MS-EVB) algorithm was used.[32] The computational expense of the SCI-MS-EVB algorithm scales linearly with N (where N is the number of hydroxides), thus making the simulation of PVBTMA systems with multiple reaction complexes feasible.

In all of the simulations presented here, the water model was the *a*SPC/Fw model developed by Park et al.[41] Periodic boundary conditions were applied to all three dimensions. In the simulations, each radial distribution function (RDF) was calculated and averaged over multiple independent runs. The mean square displacement (MSD) was calculated using the standard formula, and the self-diffusion constant was extracted from the long-time linear slope of the MSD-versus-time plot according to the Einstein relationship (eq 1):

$$\mathrm{MSD}(t) = \frac{1}{N}\left\langle \sum_{i=1}^{N} |\mathbf{r}_i(t) - \mathbf{r}_i(0)|^2 \right\rangle = 6Dt \quad (1)$$

DOI: 10.1021/jacs.5b11951
J. Am. Chem. Soc. 2016, 138, 991−1000

Because of the delocalized nature of the excess charge on OH^-, the average position of OH^- was described by the center of excess charge (CEC), which is defined as

$$\mathbf{r}_{CEC} = \sum_{i=1}^{N} c_i^2 \mathbf{r}^i_{COC} \quad (2)$$

where $\mathbf{r}^i_{COC}$ is the position vector of the center of charge of the hydroxide of the ith basis state, c_i^2 is the probability weight for the ith basis state, and N is the number of basis states.

3. RESULTS AND DISCUSSION

3.1. Models of the Bulk and PVBTMA Systems.

Hydroxide Solvation Structure. By using AIMD simulations, Tuckerman et al.[42] reported in 2002 the solvation structure of hydroxide in water, in which the OH^- accepts hydrogen bonds from four water molecules while donating one hydrogen bond to a transient water sitting directly above the hydroxide hydrogen atom (denoted as H*)[43] (Figure 2a). The hydrogen-accepting water is known to play an important role during proton transfer, a concept termed "presolvation". On the basis of the proton transfer scheme proposed in their study, the presence of such a water molecule helps to form a presolvated structure and stabilizes the newly formed water when proton transfer happens (Figure 2c).[26] These structural properties are often set as important objectives when building OH^- models,[33,44,45] and our present MS-RMD-OH model, fitted to the AIMD data, reproduces these features.

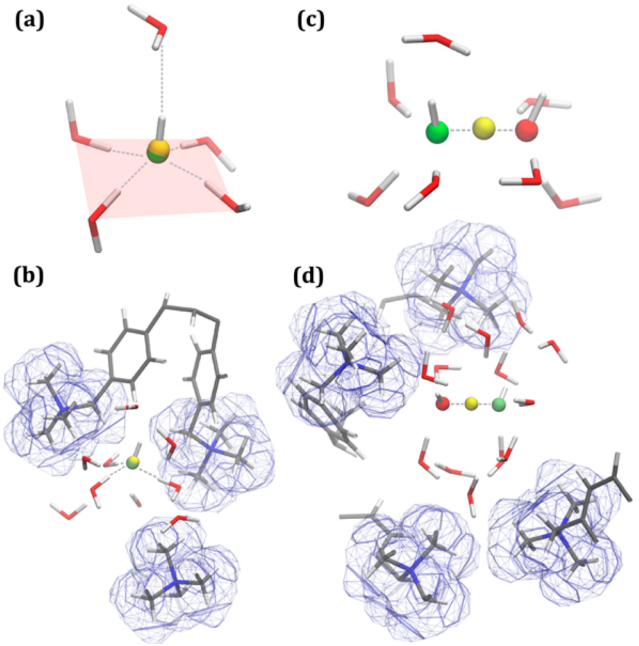

Figure 2. Snapshots of (a, b) typical solvation structures of OH^- and (c, d) the transition states of the proton transfer reactions in the (a, c) bulk water and (b, d) PVBTMA AEM systems. O* (hydroxide oxygen) is shown in green, the anionic CEC in yellow, O_w (water oxygen) in red, C in gray, N in blue, and H in white, and wireframes highlight the van der Waals surface (probe radius 1.4 Å) of QA^+ (quaternary ammonium cationic group).

In the PVBTMA case, there are clear differences in the solvation structure due to the changes in the environment (e.g., some of the coordination spots around a OH^- can be taken by quaternary ammonium cationic groups (QA^+)). In Figure 2b we show a snapshot of a typical solvation structure of OH^-, in which the OH^- is intercalated between two adjacent QA^+ groups with another QA^+ staying very close. In this configuration, the excess charge position characterized by the hydroxide CEC coincides with the O* in this state. In Figure 2d we show a snapshot of a typical configuration in which a pocket is formed by multiple QA^+ and a proton that is almost equally shared by two oxygen centers is being transferred from one water molecule to the OH^-.

Excess Anionic Charge Solvation Structure. Information about the hydration structure of the excess negative charge is important for understanding its delocalization and transport behavior. There are two commonly defined cationic structures, termed Eigen and Zundel, for a hydrated excess proton in aqueous solution. The (perfect) Eigen cation corresponds to the structure in which one hydronium ion is symmetrically solvated by three water molecules. The (perfect) Zundel cation corresponds to the configuration in which one proton is symmetrically shared by two water molecules, which represents the transition state for proton transfer. In a similar fashion, for both the bulk and PVBTMA systems, we define the configuration in which the negative charge is localized on a single OH^- as a "resting state" (Figure 2a,b) and the configuration in which a proton is almost equally shared by two oxygens as a "transition state" (Figure 2c,d).

On the basis of these definitions, we analyzed the MS-RMD probability weights for the two most probable states (c_1^2 and c_2^2) to depict in Figure 3 the delocalization of the excess anionic charge. At 300 K, the c_1^2 curve shows a single maximum at about 0.99 while the c_2^2 curve shows a single maximum at about 0.005, suggesting that the excess charge is very localized on a single hydroxide center and thus the prevailing existence of the "resting state". The lower shoulders of the c_1^2 and c_2^2 curves at around 0.5 and 0.49 respectively (Figure 3 inset) indicate a much smaller probability to observe the "transition state". As the temperature increases, there is no change in the positions of the peaks/shoulders, but we can observe an increase/decrease in the intensity of the peak/shoulder. There is no qualitative difference in these results for the bulk water and PVBTMA systems, although the former appears to have slightly more density in the shoulder region and lower density at the peaks.

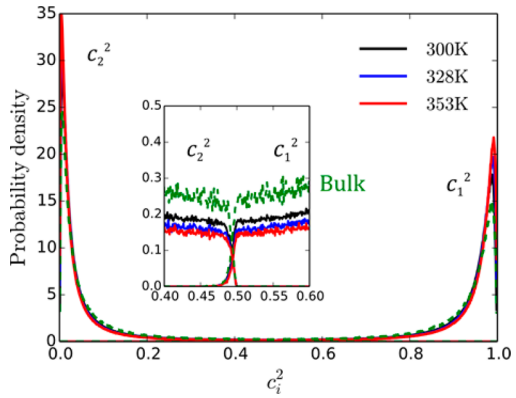

Figure 3. Probability density distributions of the largest (c_1^2) and the second largest (c_2^2) MS-RMD probability weights c_i^2 in the PVBTMA system (λ = 14) at different temperatures (300, 328, and 353 K) and in bulk water at 300 K.

Free Energy Profiles for the Proton Transfer Reaction. We also plotted the free energy profiles for the proton transfer reaction in the PVBTMA system at different temperatures as

DOI: 10.1021/jacs.5b11951
J. Am. Chem. Soc. 2016, 138, 991−1000

functions of $c_1^2 - c_2^2$ (Figure 4), which are also compared with the profile for the bulk system at 300 K. At the point $c_1^2 - c_2^2 =$ 0, the identity of the pivot state (the state having the largest probability amplitude c_i) may change, corresponding to the transition state of the proton transfer reaction. The curves show a single minimum at a $c_1^2 - c_2^2$ value of about 0.99, indicating a hydration structure with very localized charge, which is consistent with the c_1^2 distribution shown in Figure 3. At 300 K, the free energy barrier between the "resting state" and the "transition state" is about 2.8 kcal/mol, which is about 0.2 kcal/mol higher than in the bulk water case. Interestingly, an increase in temperature increases the free energy barrier, which in turn leads to a decrease in the hopping rate (Figure S7). Although the hopping rate decreases as the temperature increases, the diffusion constant (shown in the next section) still increases, implying a larger contribution from the vehicular (standard diffusive) mechanism and an improvement in the hopping transport efficiency with less nonproductive proton "rattling" behavior.

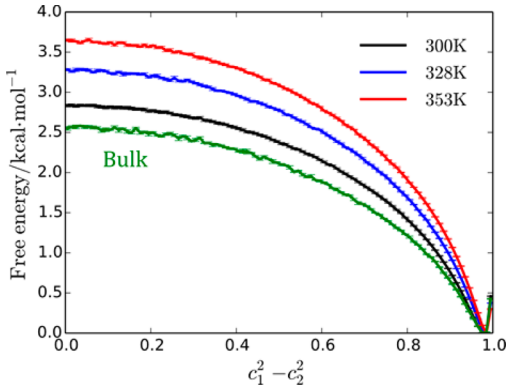

Figure 4. Free energy profiles for the proton-transfer reaction in the PVBTMA system (λ = 14) at different temperatures (300, 328, and 353 K) and in the bulk water system at 300 K as functions of the difference between the two largest probability weights ($c_1^2 - c_2^2$).

Density. To study the relationship between membrane density and water uptake, we show in Figure 5 the equilibrium density for the PVBTMA system as a function of the hydration level λ at 300 K and 1 atm. With increasing λ, the density first increases up to λ = 7 and then declines. For a relatively dry membrane, there are cavities within the material. At lower hydration levels, these cavities are filled first before the total volume changes significantly, which causes the initial increase in the system density. Once most of the cavities have been filled, absorbing more water causes the system to expand, resulting in a decrease in the density for larger λ values.

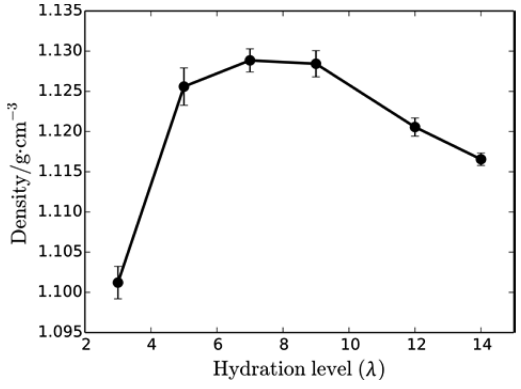

Figure 5. Density values for PVBTMA systems at different hydration levels under room conditions (300 K and 1 atm).

To help get a more global visual impression of the system, in Figure 6 we show snapshots of the PVBTMA system at 300 K using two types of representation. In Figure 6a we highlight in cyan the well-connected hydrophilic regions formed by water and OH^- and in gray the hydrophobic regions formed by the entangled polymer framework (also shown in Figure 6b). Both of them contribute to the phase segregation between the hydrophilic and hydrophobic domains, and almost all of the water and OH^- ions are included in a percolating cluster, as can be identified from the water clustering analysis shown in Figure S8.

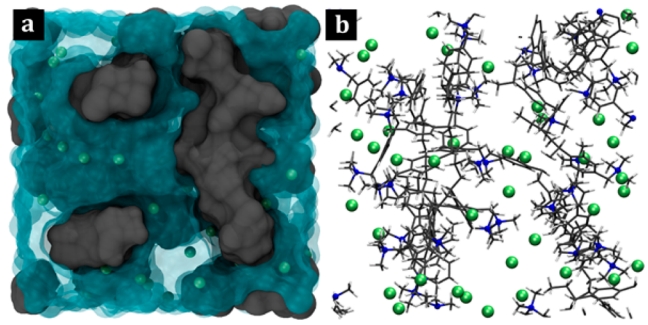

Figure 6. Snapshots of the PVBTMA system at 300 K: (a) hydrophilic region (cyan), polymer surface (gray), and OH^- (green); (b) O* (green) and polymer atoms (C, gray; H, white; N, blue).

RDFs for Hydroxide in the Bulk Water System. The quality of the model for the PVBTMA system is closely related to that for the bulk system. To show the performance of the MS-RMD-OH model, in Figure 7 we compare four RDFs from AIMD and MS-RMD simulations. The close agreement suggests that the key structural features of the system have been captured. It should be noted that instead of the CEC, the

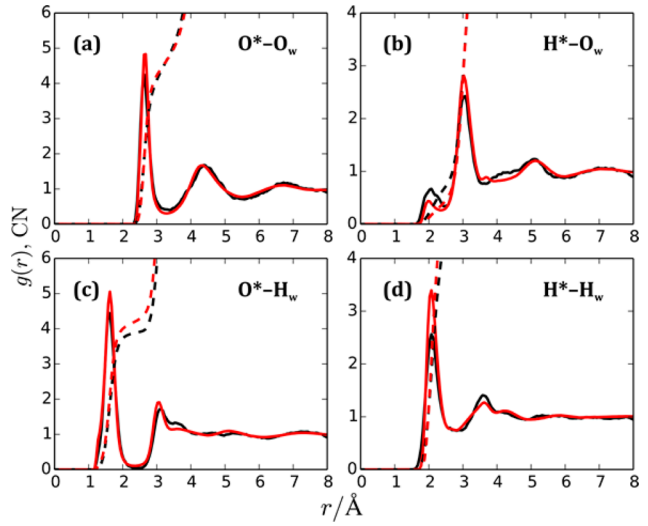

Figure 7. Comparisons of AIMD (black) and MS-RMD (red) radial distribution functions (solid lines) and integrated coordination numbers (dashed lines) between atoms of the hydroxide ion and water molecules in the bulk water system: (a) O*–O_w; (b) H*–O_w; (c) O*–H_w; (d) H*–H_w.

DOI: 10.1021/jacs.5b11951
J. Am. Chem. Soc. 2016, 138, 991−1000

O* and H* of each pivot (most hydroxide-like) state is used in the RDF comparison.

The O*−O_w (where O_w is water oxygen) RDF contains direct information about the arrangement of the water molecules around the hydroxide. The first peak includes contributions from the O_w atoms of the four hydrogen-bond-donating water neighbors and the single transient water. They add up to a total coordination number (CN) of 4.49 at r = 3.2 Å in the AIMD simulation, and our MS-RMD simulation gives a very close CN value of 4.52. Furthermore, the good agreement for both the second and third solvation shells is an improvement over a previous OH^- model.[33,45]

In the H*−O_w RDF, there is a small peak at around 2.0 Å, which corresponds to the transient water on top of the H*. As mentioned earlier, the presence of this water is important for a proton transfer reaction to happen. In our MS-RMD simulation, the position and shape of the peak are consistent with the AIMD results, although the intensity is slightly lower. The second peak contains mainly the contribution from the four hydrogen-donating water molecules, and it also includes the contribution from the nearby water.

Similarly, in the O*−H_w and H*−H_w (where H_w is water hydrogen) RDFs, the first peaks are largely contributed by the H atoms that come from the four hydrogen-donating water molecules close to O*, while the second peak is mainly contributed by the other H atoms in the four water molecules. More structural information, such as the probability distribution of the hydroxide−water oxygen angle (Figure S3) and the potential of mean force for proton transfer (Figure S4) are provided in the SI.

RDFs for Hydroxides in the PVBTMA System. Because of the variety of atom types in the PVBTMA system, in the MS-RMD-PVBTMA model we highlight only four key interactions (Figure 8): N−O*, N−H*, N−N, and O*−O_w (where N is nitrogen of a QA^+ cationic group). Additional RDFs are provided in Figure S6. The N−O* and N−H* RDFs contain information about the solvation of the cationic group by hydroxide, whereas the N−N RDF displays the self-distribution of N and the O*−O_w RDF characterizes the solvation of O* by O_w in the material.

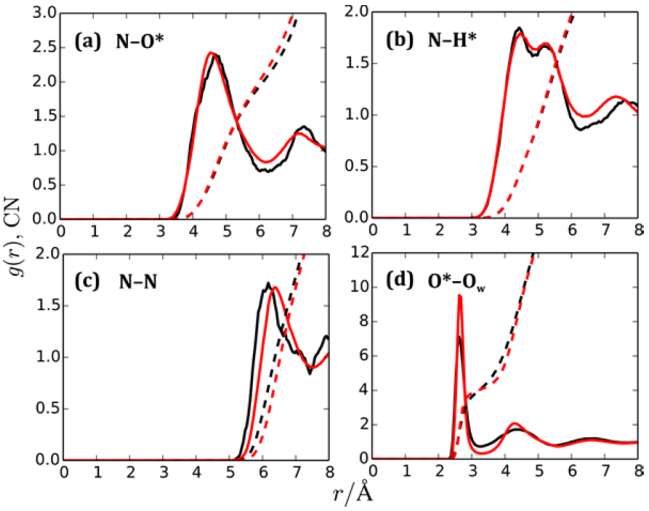

Figure 8. Comparison of AIMD (black) and MS-RMD (red) RDFs (solid lines) and CNs (dashed lines) in the PVBTMA system: (a) N−O*; (b) N−H*; (c) N−N; (d) O*−O_w.

As shown in Figure 8, both the N−O* and N−H* RDFs are well-reproduced, and similar parametrization was also found to improve the RDFs in our previous study on 3M and Hyflon PEMs.[31] These additional parametrizations of the interactions between the mobile ions and the charged tethered groups in both PEM and AEM systems are found to be important. When the standard Lorentz−Berthelot mixing rules are used for the LJ interactions, oversticking between the oppositely charged species can sometimes happen. Such reparametrization helps to resolve the oversticking problem and better reproduce the RDFs from the AIMD reference data.

The N−O* RDF shows two clear peaks, corresponding to the first and second hydration shells. The N−O* CN gives a number as high as 2.2 at a distance of 6.1 Å (the end of the first hydration shell). This means that there are more than two OH^- anions on average in the first shell of each N. In other words, each OH^- is on average attached to more than two N atoms, which also implicitly suggests an overlap between the first solvation shells of neighboring side chains.

The N−N RDFs show good agreement between the MS-RMD and AIMD simulations in regard to the intensity, although the first peak is slightly shifted to a larger distance. It is clear that adjacent N atoms are separated in a rather regular pattern, as can be seen from the relatively sharp first peak and the coordination number greater than 2.0 at r = 7.3 Å (the end of first hydration shell).

In the O*−O_w RDF, compared with the AIMD reference, we observed a slightly more structured solvation structure for OH^-, and the CN value for hydroxide (estimated at 3.1 Å) was calculated to be 3.93, which is very close to the AIMD reference value of 3.80. Compared with the bulk case, this CN value is smaller by about 0.6−0.7 because some of the spots around the OH^- have been taken by other species such as QA^+.

Diffusion of Hydroxide in the Bulk Water System. With the present MS-RMD-OH bulk model, we calculated the hydroxide mean square displacement (MSD) for a system that contains a single OH^- in water (see Figure S5). The hydroxide self-diffusion constant was calculated to be 0.22 ± 0.04 $Å^2$/ps at 300 K, which is about 42% of the experimental value of 0.53 $Å^2$/ps.[46] The present model does not include explicit nuclear quantum effects, which have been found to approximately double the diffusion in the hydrated excess proton case.[47−49] The total temperature drift is 0.64 ± 0.12 K/ns, and the energy drift is 3.5 ± 0.7 kcal mol^{-1} ns^{-1}, which is slightly better than in our previous OH^- model (5.8 ± 4.8 kcal mol^{-1} ns^{-1}).[33]

With these reasonable hydroxide models (MS-RMD-OH and MS-RMD-PVBTMA) developed for the bulk water and PVBTMA systems, we will propose below a transport mechanism for hydroxide in the AEM from the structural and dynamical properties that are discussed next.

3.2. Additional Solvation Features in the PVBTMA System and the Hydroxide Transport Mechanism.

Relative Position of QA^+ and OH^-. We learned from the N−O* RDF that the first hydration shell of O* around N is centered at about 4.6 Å and distributed in the range from about 3.5 to 6.1 Å, but this does not contain information on the orientation of OH^- relative to QA^+. In Figure 9a we show the joint probability density between the N−O* distance (d) and the C_{CH_2}−N−O* angle (θ), where C_{CH_2} is the methylene carbon connected to N. This probability density plot provides us with information about which relative positions around the N atom are preferred by the hydroxide O*. The graph can be

DOI: 10.1021/jacs.5b11951
J. Am. Chem. Soc. 2016, 138, 991−1000

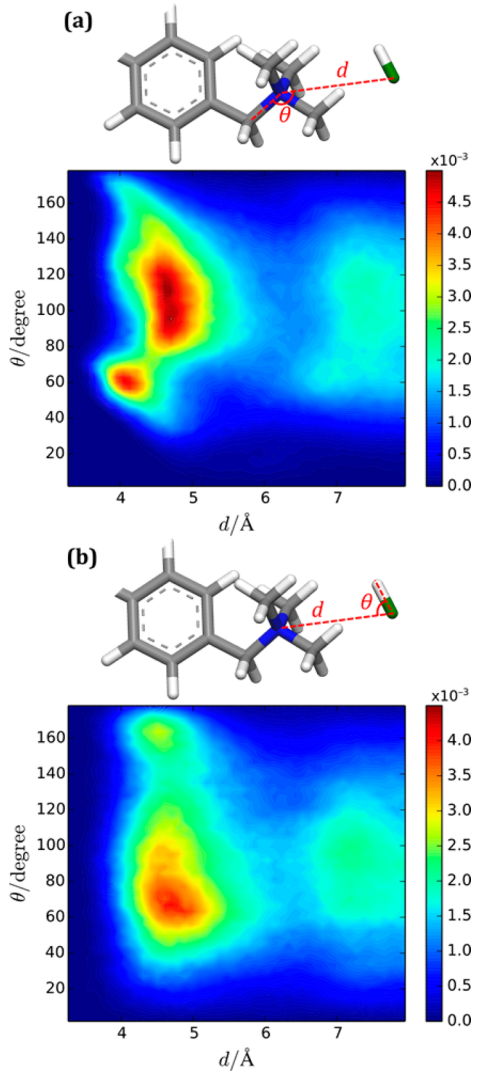

Figure 9. Joint probability density distributions of (a) the N−O* distance (d) and the C_{CH_2}−N−O* angle (θ) and (b) the N−O* distance (d) and the H*−O*−N angle (θ) for the PVBTMA system (λ = 14) at 300 K. In both graphs, the probability densities are scaled by $4\pi d^2$ to account for the spherical shell volume, as in an RDF calculation. The bin size for θ is 3.6°, and that for d is 0.1 Å.

roughly divided into two parts at d = 6.1 Å, with the left reflecting the first coordination shell and the right the second shell. The higher densities for 80° < θ < 130° suggest the preference of O* for positions around the methyl groups of QA^+, and the more separated red region at $\theta \approx 60°$ indicates a probable spot next to the methylene group of QA^+. One plausible reason for this preference is that the H atoms of the methylene group are slightly more positively charged than those on methyl groups around N (see Figure S1). Another possible reason is the lower steric hindrance at that position. More importantly, the fact that the N−N distance is relatively short makes it even more probable when one OH^- stays between two adjacent QA^+.

While we have shown that OH^- prefers the position at the side of QA^+, we are also interested in knowing the orientation of the O*−H* bond relative to the nitrogen position. As shown in Figure 9b, we calculated the joint probability density between the N−O* distance and another angle, H*−O*−N, which shows a slight preference for $\theta \approx 70°$ in the first shell. For both of the joint probability density distributions discussed above, an increase in temperature does not make a significant difference.

On the basis of the RDFs and the two probability distribution plots, we are able to construct a visual picture of the relative position of QA^+ and OH^-. Moreover, the OH^- has substantial freedom to explore around the QA^+, as can be seen from the spread in the probability density distribution for a large range of θ.

Self-Diffusion Constants and Their Components. The self-diffusion constants, D, are listed in Table S5 and shown in Figure 10 as an Arrhenius plot. These self-diffusion constants

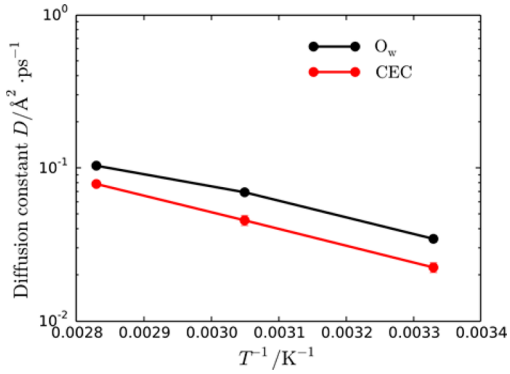

Figure 10. Self-diffusion constants (on a log scale) of hydroxide CEC and water O_w as functions of $1/T$ for the PVBTMA system at hydration level λ = 14.

were calculated from the long-time slopes of the MSD curves for the hydroxide CEC and water O_w at different temperatures, as shown in Figure 11. For both the hydroxide CEC and water O_w, the diffusion becomes faster as temperature increases, as expected. The activation energy, ΔE_a, for the hydroxide CEC self-diffusion in the PVBTMA system was calculated to be 4.97 kcal/mol, in good agreement with the experimental value of 4.54 ± 0.24 kcal/mol obtained from conductivity measurements.[38]

Because of the Grotthuss hopping mechanism, it is useful to decompose the total MSD of the CEC into "discrete" and "continuous" components,[29,30] and the results reveal how much each component contributes. The formula for the decomposition can be represented by eqs 3 and 4 as

$$\mathbf{r}_{CEC}(t) - \mathbf{r}_{CEC}(0) = \Delta\mathbf{r}_{CEC}(t) = \Delta\mathbf{r}_d(t) + \Delta\mathbf{r}_c(t) \quad (3)$$

$$\langle|\Delta\mathbf{r}_{CEC}(t)|^2\rangle = \langle|\Delta\mathbf{r}_d(t)|^2\rangle + \langle|\Delta\mathbf{r}_c(t)|^2\rangle + 2\langle\Delta\mathbf{r}_d(t)\cdot\Delta\mathbf{r}_c(t)\rangle \quad (4)$$

where $\Delta\mathbf{r}_d(t)$ and $\Delta\mathbf{r}_c(t)$ are the discrete (hopping) and continuous (vehicular) components of the hydroxide CEC displacements, respectively, and $\langle|\Delta\mathbf{r}_{CEC}(t)|^2\rangle$, $\langle|\Delta\mathbf{r}_d(t)|^2\rangle$, and $\langle|\Delta\mathbf{r}_c(t)|^2\rangle$ are the MSDs of the total, discrete, and continuous displacements, respectively, with $\Delta\mathbf{r}_d(0) = \Delta\mathbf{r}_c(0) = 0$.

In this discrete−continuous (D−C) decomposition, we examined every 100 fs interval to see whether there was any hopping for each hydroxide CEC, which happens when there is a change in the identity of the pivot state (the most hydroxide-like structure). If the CEC hopped within an interval, no matter whether the pivot state changed identity or not at the end of the 100 fs, the CEC displacement in the interval was assigned to the discrete component and a value of 0 was simultaneously

DOI: 10.1021/jacs.5b11951
J. Am. Chem. Soc. 2016, 138, 991−1000

assigned to the continuous component. If no hopping occurred in the interval, the displacement was assigned to the continuous component and a value of 0 was assigned to the discrete component.

Figure 11a shows the full MSD for the hydroxide CEC as well as the decomposed discrete and continuous components.

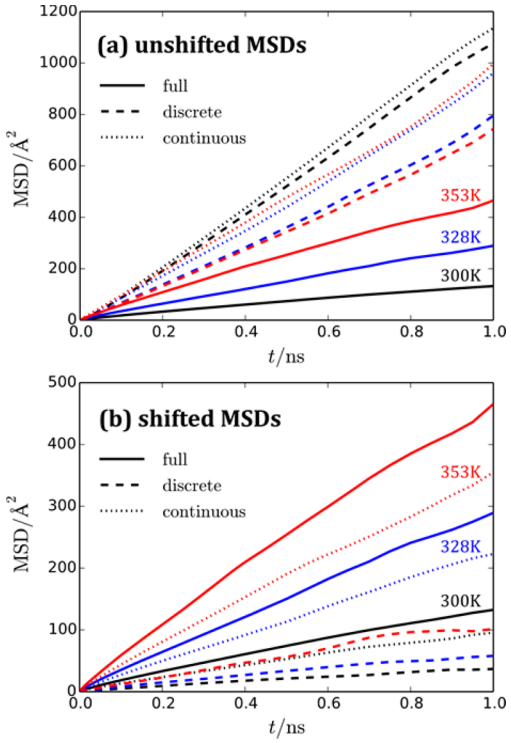

Figure 11. Full MSD of the hydroxide CEC and its decomposition into discrete and continuous MSD components for the PVBTMA system (λ = 14) at different temperatures (300, 328, and 353 K). Both the (a) unshifted and (b) shifted MSDs are shown.

It is clear that both components are considerably larger than the full MSD, which implies an anticorrelation between the components. In other words, the vector dot-product term $\langle \Delta \mathbf{r}_c(t) \cdot \Delta \mathbf{r}_d(t) \rangle$ in eq 4 is negative because the discrete and continuous motions tend to move at times in directions greater than 90° from each other (even opposite to each other, i.e., 180°). Such anticorrelation of the diffusive components was observed first for hydrated proton diffusion in PEM systems such as Nafion,[29,50,51] Hyflon, and 3M[30] and is further seen here for hydroxide diffusion in the AEM.

The magnitude of the anticorrelation term can be so large that the change in each component is washed out. In order to analyze the discrete and continuous components more completely, we added one-half of the anticorrelation term to each component to obtain the "shifted" decomposed MSDs (eq 5),

$$\begin{aligned} \langle |\Delta \mathbf{r}_{CEC}(t)|^2 \rangle &= [\langle |\Delta \mathbf{r}_d(t)|^2 \rangle + \langle \Delta \mathbf{r}_d(t) \cdot \Delta \mathbf{r}_c(t) \rangle] \\ &\quad + [\langle |\Delta \mathbf{r}_c(t)|^2 \rangle + \langle \Delta \mathbf{r}_d(t) \cdot \Delta \mathbf{r}_c(t) \rangle] \\ &= \text{shiftedMSD}_d + \text{shiftedMSD}_c \end{aligned} \quad (5)$$

which are plotted in Figure 11b. Both the unshifted and shifted decomposed MSDs show a larger contribution from the continuous component than the discrete component. This is partly because the frequency of discrete motion is less than that of continuous motion. However, even with a lower frequency, the discrete component contributes significantly to the total MSD, pointing to the importance of the Grotthuss mechanism in these hydroxide AEM systems.

In addition to the D−C decomposition, another way to decompose the full MSD is by separating it into individual MSD components for "associated" or "free" OH^-.[31] In the free−associated (F−A) decomposition, we again considered individual 100 fs intervals. However, if the OH^- was associated with any QA^+ group (distance less than 6.1 Å, which constitutes the first coordination shell of a QA^+ group) at any point within an interval, this MSD contribution was assigned to the associated component for the interval while simultaneously a value of 0 was assigned to the free component. If the OH^- was completely free in an interval, the MSD contribution for this interval was assigned to the free component while simultaneously a value of 0 was assigned to the associated component. A threshold value t^* = 2 ps (inclusive) was chosen here in order to alleviate the influence of frequent proton "rattling" events. Our criterion was that if one hydroxide CEC escaped from the domain but reentered within this t^* interval, it was considered as associated during this time. Following this criterion, the mean residence times of OH^- around QA^+ groups at 300, 328, and 355 K were calculated to be 14.1 ± 0.2, 12.9 ± 0.2, and 11.5 ± 0.2 ps, respectively.

The F−A decomposition results are shown in Figure 12b. Similar to the unshifted plots (Figure 12a), there is also anticorrelation between the free and associated components, but the relative magnitude is much smaller than that of the D−C decomposition case. It is not particularly surprising to see

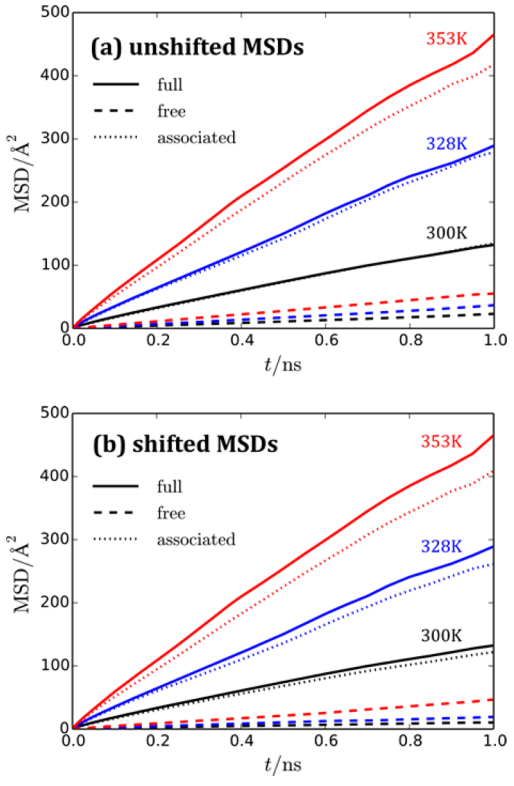

Figure 12. Full MSD of the hydroxide CEC and its decomposition into free and associated MSD components for the PVBTMA system (λ = 14) at different temperatures (300, 328, and 353 K). Both (a) unshifted and (b) shifted MSDs are shown.

DOI: 10.1021/jacs.5b11951
J. Am. Chem. Soc. 2016, 138, 991−1000

that the total MSD is contributed almost completely by the associated components because in most cases hydroxide CECs are associated with multiple QA^+ groups, as was mentioned earlier, and this also explains why the magnitude of the anticorrelation term is small. This structural feature becomes clearer if we calculate the fraction of O atoms from water and OH^- that are not associated with the first hydration shell of any N atom, which gives the values as 9.87%, 9.95%, and 11.1% at 300, 328, and 353 K, respectively. This means that about 90% of the water and OH^- ions are associated with at least one QA^+ group, and this is responsible for the predominant contribution from the associated components. *Thus, most of the anionic charges are transported within the surface domain formed by the overlapping first solvation shells of the AEM QA^+ groups.*

Conformations of Side Chains. In PVBTMA, each QA^+ group is at the end of a side chain, which is attached to the polymer backbone. The flexibility of the side chains and the induced motion of the tethered charges were considered in our previous studies of PEMs.[30,31] To characterize the flexibility, in Figure 13 we show a joint probability density distribution

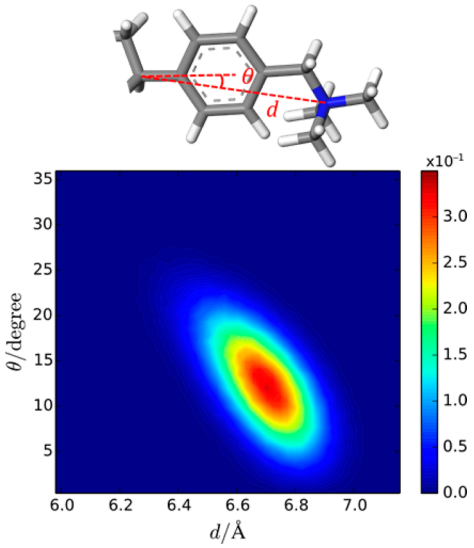

Figure 13. Joint probability density distribution of d and θ for the PVBTMA system at hydration level $\lambda = 14$. The bin size for θ is 0.7°, and that for d is 0.04 Å.

between d and θ, where d is the distance between the N atom and the backbone C atom to which the side chain is connected and θ is the angle indicated at the top of Figure 13. Here we show only the results for the PVBTMA system at 300 K because the results at the different temperatures are similar. The graph clearly shows a unimodal distribution, and the localized probability density indicates the inflexible nature of the side chain for this AEM. This is consistent with the molecular structure of the material, which consists of relatively short side chains and rigid benzene rings.

However, it is important to note that although the side chains are rather inflexible, the short backbone repeating unit (only two carbon atoms) allows two QA^+ groups from adjacent side chains to be so close to each other that their first solvent coordination shells are well overlapped. This is clear by looking at the range of the first peak in the RDFs for N−O* (from 3.5 to 6.1 Å; Figure 8a) and N−N (from 5.5 to 7.5 Å; Figure 8c). A schematic diagram with the value of the center of the first peak from the two RDFs illustrates this possible overlap (Figure 14).

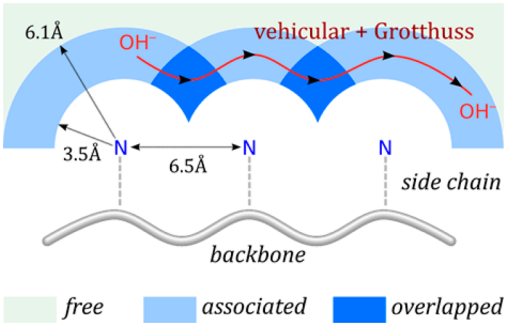

Figure 14. Schematic of the proposed mechanism for OH^- transport in the PVBTMA AEM system.

The significant overlap suggests that in order to be transported along the surface formed by a series of closely and well-separated QA^+ groups, the OH^- does not have to take a two-step motion in which it leaves one QA^+ and joins another. *Instead, it can move continuously along the surface formed by the QA^+ groups.*

4. CONCLUSIONS

In this work, using AIMD reference data, we have parametrized a new reactive OH^- MD model in bulk water and also constructed a reactive OH^- model for the PVBTMA AEM material. Both models are shown to reproduce the properties of the AIMD simulations quite well. The subsequent long-time-scale MS-RMD simulations for PVBTMA revealed the OH^- transport mechanism in the PVBTMA AEM system (cf. Figure 14): Throughout the membrane, the regularly spaced rigid side chains form a regular distribution of QA^+ groups. The first coordination shells of QA^+ are close enough to have considerable overlap with each other, forming continuous surface regions for OH^- transport. The OH^- anions show a slight preference for the sites within the overlap of neighboring coordination shells and also have sufficient freedom to migrate. The transport of OH^- happens mostly in the confined surface domain, where both the vehicular and Grotthuss mechanisms make significant contributions.

For the hydroxide hydration structure, we observed that for the bulk (hydroxide) system the probability weights c_1^2 and c_2^2 show maxima at 0.99 and 0.005, respectively (see Figure 3), and the intensity of the c_1^2 peak is as high as about 15, indicating a rather localized charge distribution. By contrast, in the case of the bulk water hydrated excess proton,[49] the excess charge is more delocalized, with maxima in c_1^2 and c_2^2 appearing at about 0.6 and 0.13, respectively. The intensity of the c_1^2 peak in the case of the hydrated excess proton is about 7, implying a larger probability for the formation of the transition state (Zundel cation). The more localized nature of the excess charge in the bulk water hydroxide system is correlated with a higher free energy barrier between the "resting state" and "transition state" (~2.6 kcal/mol for hydroxide (Figure 4) vs ~1.0 kcal/mol for proton[49]) and a lower hopping rate for the bulk hydroxide system than the bulk excess proton system. The free energy barrier and hopping rate also have a large effect on the relative contributions of the vehicular and Grotthuss mechanisms to the self-diffusion. More specifically, we observed a considerably larger "continuous" MSD component than the "discrete" MSD component in the PVBTMA system, while our previous studies of proton transport in PEMs found a slightly larger contribution from the "discrete" MSD component than the

DOI: 10.1021/jacs.5b11951
J. Am. Chem. Soc. 2016, 138, 991−1000

"continuous" MSD component. Consequently, for the two classes of polymer electrolytes there is qualitative difference in the contribution from the Grotthuss hopping mechanism (correlated with the "discrete" component) and vehicular mechanism (correlated with the "continuous" component).

There is also another important difference in the polymer structures of PVBTMA and PEMs. For instance, the 3M membrane (equivalent weight 825)[30,31] is a PEM material that contains 10 carbon atoms (besides the fluorine atoms) in the backbone for each repeat unit, while PVBTMA contains many fewer carbon atoms (typically two), suggesting a much shorter distance between adjacent side chains in PVBTMA. In addition, PVBTMA has a less flexible side chain than the 3M membrane, which can be identified by comparing Figure 13 with the similar analysis in our previous studies.[30,31] In the PVBTMA system, the short distance between adjacent side chains and the lower flexibility form a close and regular distribution of cation groups, which allows the first coordination shells of adjacent tethered charged groups to overlap well. In the 3M membrane, despite the larger distances between the side chains, these long and flexible side chains are able to move the tethered charged groups into closer contact, and thus, their first coordination shells can also overlap well. In the 3M membrane, charged groups carry the protons in their coordination shells, and protons can be transferred from one tethered charged group to another in the overlapped region. In PVBTMA, the OH^- can also be transported between the charged groups, but the difference is that OH^- would not need to wait for the side chains to significantly move and meet each other. This behavior may provide an advantage for the anion transport and could prove to be important as an AEM design principle.

Finally, the calculated activation energy ΔE_a for hydroxide CEC self-diffusion agrees well with that obtained from conductivity experiments[38] and is larger than the ΔE_a for the excess proton CEC in Nafion.[50] Generally, in experiments AEMs are found to show lower conductivity than PEMs, which is consistent with a comparison of the ion self-diffusion constants from the present PVBTMA results and our previous PEM studies.[29−31,50,52] However, a larger ΔE_a value for the present AEM than the typical PEM materials suggests that elevated temperatures will improve transport more greatly in AEMs than in PEMs. This could also be of significance for AEM fuel cell design and applications.

■ ASSOCIATED CONTENT

Supporting Information

The Supporting Information is available free of charge on the ACS Publications website at DOI: 10.1021/jacs.5b11951.

More details about methodology, parametrization, and simulation as well as additional characterization results for both the MS-RMD-OH and MS-RMD-PVBTMA models (PDF)

■ AUTHOR INFORMATION

Corresponding Author

*gavoth@uchicago.edu

Present Address

⊥Y.-L.S.T.: Department of Chemistry, The Chinese University of Hong Kong, Shatin, New Territories, Hong Kong.

Notes

The authors declare no competing financial interest.

■ ACKNOWLEDGMENTS

The research was funded by the Army Research Office through a Multidisciplinary University Research Initiative (MURI) Grant under Contract W911NF-10-1-0520. C.C. is grateful for the financial support from National Natural Science Foundation of China (Grants 21303123 and 21303124) and the China Scholarship Council (201306275019). Y.-L.S.T. acknowledges the Croucher Foundation for a postdoctoral research fellowship. We are grateful to the members of the Anionic Transport in Organic Media MURI team for numerous fruitful discussions and support. This research used resources of the Argonne Leadership Computing Facility (ALCF), which is a DOE Office of Science User Facility supported under Contract DE-AC02-06CH11357. An award of computer time was provided by ALCF's Director's Discretionary Program. The computational resources in this work were also provided in part by a grant of computer time from the U.S. Department of Defense (DOD) High Performance Computing Modernization Program at the Engineer Research and Development Center (ERDC) and in part by the University of Chicago Research Computing Center (RCC).

■ REFERENCES

(1) Varcoe, J. R.; Slade, R. C. T. *Fuel Cells* **2005**, *5*, 187.
(2) Varcoe, J. R.; Atanassov, P.; Dekel, D. R.; Herring, A. M.; Hickner, M. A.; Kohl, P. A.; Kucernak, A. R.; Mustain, W. E.; Nijmeijer, K.; Scott, K.; Xu, T. W.; Zhuang, L. *Energy Environ. Sci.* **2014**, *7*, 3135.
(3) Hickner, M. A.; Herring, A. M.; Coughlin, E. B. *J. Polym. Sci., Part B: Polym. Phys.* **2013**, *51*, 1727.
(4) Mauritz, K. A.; Moore, R. B. *Chem. Rev.* **2004**, *104*, 4535.
(5) Debe, M. K. *Nature* **2012**, *486*, 43.
(6) Jacobson, M. Z.; Colella, W. G.; Golden, D. M. *Science* **2005**, *308*, 1901.
(7) Zhang, J.; Sasaki, K.; Sutter, E.; Adzic, R. R. *Science* **2007**, *315*, 220.
(8) Pan, J.; Chen, C.; Zhuang, L.; Lu, J. *Acc. Chem. Res.* **2012**, *45*, 473.
(9) Lu, S. F.; Pan, J.; Huang, A. B.; Zhuang, L.; Lu, J. T. *Proc. Natl. Acad. Sci. U. S. A.* **2008**, *105*, 20611.
(10) Asazawa, K.; Yamada, K.; Tanaka, H.; Oka, A.; Taniguchi, M.; Kobayashi, T. *Angew. Chem., Int. Ed.* **2007**, *46*, 8024.
(11) Gu, S.; Cai, R.; Luo, T.; Chen, Z.; Sun, M.; Liu, Y.; He, G.; Yan, Y. *Angew. Chem., Int. Ed.* **2009**, *48*, 6499.
(12) Zhang, H.; Shen, P. K. *Chem. Rev.* **2012**, *112*, 2780.
(13) Wang, Y. J.; Qiao, J.; Baker, R.; Zhang, J. *Chem. Soc. Rev.* **2013**, *42*, 5768.
(14) Kreuer, K. D. *Chem. Mater.* **2014**, *26*, 361.
(15) Merle, G.; Wessling, M.; Nijmeijer, K. *J. Membr. Sci.* **2011**, *377*, 1.
(16) Elliott, J. A.; Paddison, S. J. *Phys. Chem. Chem. Phys.* **2007**, *9*, 2602.
(17) Schmidt-Rohr, K.; Chen, Q. *Nat. Mater.* **2008**, *7*, 75.
(18) Shah, A. A.; Luo, K. H.; Ralph, T. R.; Walsh, F. C. *Electrochim. Acta* **2011**, *56*, 3731.
(19) Jorn, R.; Savage, J.; Voth, G. A. *Acc. Chem. Res.* **2012**, *45*, 2002.
(20) Pan, J.; Chen, C.; Li, Y.; Wang, L.; Tan, L. S.; Li, G. W.; Tang, X.; Xiao, L.; Lu, J. T.; Zhuang, L. *Energy Environ. Sci.* **2014**, *7*, 354.
(21) Tse, Y.-L. S.; Sarode, H. N.; Lindberg, G. E.; Witten, T. A.; Yang, Y.; Herring, A. M.; Voth, G. A. *J. Phys. Chem. C* **2014**, *118*, 845.
(22) Tse, Y. L.; Voth, G. A.; Witten, T. A. *J. Chem. Phys.* **2015**, *142*, 184905.
(23) Han, K. W.; Ko, K. H.; Abu-Hakmeh, K.; Bae, C.; Sohn, Y. J.; Jang, S. S. *J. Phys. Chem. C* **2014**, *118*, 12577.
(24) Herbst, D. C.; Witten, T. A.; Tsai, T. H.; Coughlin, E. B.; Maes, A. M.; Herring, A. M. *J. Chem. Phys.* **2015**, *142*, 114906.
(25) Agmon, N. *Chem. Phys. Lett.* **1995**, *244*, 456.

DOI: 10.1021/jacs.5b11951
J. Am. Chem. Soc. 2016, 138, 991−1000

(26) Marx, D.; Chandra, A.; Tuckerman, M. E. *Chem. Rev.* **2010**, *110*, 2174.
(27) Voth, G. A. *Acc. Chem. Res.* **2006**, *39*, 143.
(28) Swanson, J. M.; Maupin, C. M.; Chen, H.; Petersen, M. K.; Xu, J.; Wu, Y.; Voth, G. A. *J. Phys. Chem. B* **2007**, *111*, 4300.
(29) Petersen, M. K.; Voth, G. A. *J. Phys. Chem. B* **2006**, *110*, 18594.
(30) Tse, Y. L. S.; Herring, A. M.; Kim, K.; Voth, G. A. *J. Phys. Chem. C* **2013**, *117*, 8079.
(31) Savage, J.; Tse, Y. L. S.; Voth, G. A. *J. Phys. Chem. C* **2014**, *118*, 17436.
(32) Wang, F.; Voth, G. A. *J. Chem. Phys.* **2005**, *122*, 144105.
(33) Knight, C.; Lindberg, G. E.; Voth, G. A. *J. Chem. Phys.* **2012**, *137*, 22A525.
(34) Wang, J.; Wolf, R. M.; Caldwell, J. W.; Kollman, P. A.; Case, D. A. *J. Comput. Chem.* **2004**, *25*, 1157.
(35) Tsai, T.-H.; Maes, A. M.; Vandiver, M. A.; Versek, C.; Seifert, S.; Tuominen, M.; Liberatore, M. W.; Herring, A. M.; Coughlin, E. B. *J. Polym. Sci., Part B: Polym. Phys.* **2013**, *51*, 1751.
(36) Vandiver, M. A.; Caire, B. R.; Poskin, Z.; Li, Y.; Seifert, S.; Knauss, D. M.; Herring, A. M.; Liberatore, M. W. *J. Appl. Polym. Sci.* **2015**, *132*, 41596.
(37) Vandiver, M. A.; Caire, B. R.; Ertem, S. P.; Tsai, T. H.; Coughlin, E. B.; Herring, A. M.; Liberatore, M. W. *J. Electrochem. Soc.* **2015**, *162*, H206.
(38) Pandey, T. P.; Maes, A. M.; Sarode, H. N.; Peters, B. D.; Lavina, S.; Vezzu, K.; Yang, Y.; Poynton, S. D.; Varcoe, J. R.; Seifert, S.; Liberatore, M. W.; Di Noto, V.; Herring, A. M. *Phys. Chem. Chem. Phys.* **2015**, *17*, 4367.
(39) Plimpton, S. *J. Comput. Phys.* **1995**, *117*, 1.
(40) Humphrey, W.; Dalke, A.; Schulten, K. *J. Mol. Graphics* **1996**, *14*, 33.
(41) Park, K.; Lin, W.; Paesani, F. *J. Phys. Chem. B* **2012**, *116*, 343.
(42) Tuckerman, M. E.; Marx, D.; Parrinello, M. *Nature* **2002**, *417*, 925.
(43) O* and H* are the hydroxide oxygen and hydrogen, respectively. In MS-RMD, these represent the hydroxide oxygen and hydrogen in the most probable state, or "pivot state".
(44) Ufimtsev, I. S.; Kalinichev, A. G.; Martinez, T. J.; Kirkpatrick, R. J. *Chem. Phys. Lett.* **2007**, *442*, 128.
(45) Knight, C.; Voth, G. A. *Mol. Phys.* **2012**, *110*, 935.
(46) Atkins, P.; de Paula, J. *Atkins' Physical Chemistry*, 8th ed.; Oxford University Press: Oxford, U.K., 2006.
(47) Schmitt, U. W.; Voth, G. A. *J. Chem. Phys.* **1999**, *111*, 9361.
(48) Schmitt, U. W.; Voth, G. A. *Chem. Phys. Lett.* **2000**, *329*, 36.
(49) Wu, Y.; Chen, H.; Wang, F.; Paesani, F.; Voth, G. A. *J. Phys. Chem. B* **2008**, *112*, 7146.
(50) Feng, S.; Voth, G. A. *J. Phys. Chem. B* **2011**, *115*, 5903.
(51) Feng, S.; Voth, G. A. *J. Phys. Chem. B* **2011**, *115*, 10570.
(52) Savage, J.; Voth, G. A. *J. Phys. Chem. Lett.* **2014**, *5*, 3037.

DOI: 10.1021/jacs.5b11951
J. Am. Chem. Soc. 2016, 138, 991−1000